Airborne Radio Frequency Interference Studies at C-band using a Digital Receiver

J. T. Johnson, A. J. Gasiewski, B. Guner, G. A. Hampson, S. W. Ellingson, R. Krishnamachari, N. Niamsuwan, E. McIntyre, M. Klein, and V. Leuski

***Abstract*— Corruption of C-band microwave brightness observations by radio frequency interference (RFI) has been reported in recent data from orbiting radiometers; methods for mitigating these effects are of great importance for the design of future spaceborne microwave radiometers. One approach that has been suggested involves the use of multiple sub-channels at C-band as opposed to a single channel; the use of multiple sub-channels allows RFI to be detected and mitigated by analyzing relationships among sub-channel brightnesses. While this approach has been utilized in previous airborne measurements, demonstrations of the RFI mitigation performance achieved have been difficult to obtain.**

To address this issue, an enhanced airborne system for observing radio frequency interference effects on C-band microwave radiometers was developed, and is described in this paper. The system includes a traditional microwave radiometer with four C-band sub-channels, so that RFI removal is possible using a sub-channel mitigation algorithm. In addition, the system includes a digital receiver with the capability of providing high temporal and spectral resolution observations of interference. This high resolution data allows improved understanding of RFI sources to be obtained, and also allows analysis of sub-channel mitigation algorithm performance.

Observations using the system in a test flight near Wallops Island, VA are described. Results show the four sub-channel approach generally to be effective in mitigating the observed RFI sources, although examples are also illustrated using the digital receiver data to demonstrate failure of this approach. While studies of the digital receiver data alone could be performed to demonstrate further improvements in RFI mitigation, issues with this initial dataset limit the extent of such studies. Nevertheless, the results obtained still demonstrate qualitatively the improved RFI mitigation that can be achieved in brightness observations through the use of digital receivers.

***Index Terms*— Microwave Radiometry, Radio Frequency Interference**

I. Introduction

THE absence of a protected portion of the spectrum at C-band [1] makes radio frequency interference (RFI) a major concern for C-band microwave radiometry. The C-band channel of the AMSR-E radiometer on the AQUA satellite has already shown major corruption of data over a large percentage of global land mass [2]. Recent data from the WindSat satellite [3]-[4] also shows significant corruption of the C-band channel. C-band channels remain highly desirable however due to their improved sensitivity to soil moisture, sea surface temperature, and other environmental parameters compared to higher frequency channels. The CMIS instrument of the NPOESS generation of satellites includes a C-band channel [5], but clearly some form of RFI mitigation will be required in order to produce reliable C-band data [6]. Possible strategies include the use of multiple frequency channels as opposed to a single channel [7], more rapid time sampling of the incoming data, or the use of digital receiver technologies to achieve improved RFI resolution both in time and frequency. While such strategies have been applied in radio astronomy for some time [8], predicting the performance of these approaches for Earth observations is difficult without a detailed understanding of the existing RFI environment.

To address this issue, a combined analog/digital radiometer for airborne experiments was designed and developed through a collaboration of NOAA/ETL and The Ohio State University. The radiometer is based on the Polarimetric Scanning Radiometer/CX (PSR/CX) of NOAA/ETL, with the addition of a new downconversion section so that tuned radiometric observations throughout C-band are possible. A portion of the IF signal after downconversion is coupled to a digital receiver developed at Ohio State; the combined PSR and digital backend system is termed the C-band interference suppressing radiometer, or CISR, in what follows. CISR is capable of providing highly detailed information on RFI properties as well as implementing simple RFI mitigation strategies in real time.

The next section of the paper provides a brief discussion of RFI issues for traditional microwave radiometers, while Sections III and IV describe a basic block diagram of the system developed and the digital receiver subsystem, respectively. Experiments involving observations near Wallops Island, VA are described in Section V, and results are summarized in Section VI.

II. RFI Issues for Microwave Radiometers

The design of a traditional microwave radiometer is based on the assumption that the observed signal consists only of thermal noise. Because the goal of radiometry is to estimate

Manuscript received Month dd, yyyy; revised Month dd, yyyy. This work was supported by the National Polar-orbiting Operational Environmental Satellite System Integrated Program Office and the Naval Research Laboratory.

J. T. Johnson, B. Guner, R. Krishnamachari, and N. Niamsuwan are with the Dept. of Electrical and Computer Engineering and ElectroScience Laboratory, The Ohio State University (Email: johnson@ee.eng.ohio-state.edu).

A. J. Gasiewski, E. McIntyre, M. Klein, and V. Leuski are with NOAA Environmental Technology Laboratory (Email: al.gasiewski@noaa.gov).

S. W. Ellingson is with the Department of Electrical and Computer Engineering, Virginia Tech (Email: ellingson@vt.edu)

G. Hampson was with the Dept. of Electrical and Computer Engineering and ElectroScience Laboratory, The Ohio State University, and is now with the Australia Telescope National Facility.

accurately the mean power of the incoming thermal noise, integration periods on the order of milliseconds or longer are desirable in order to reduce uncertainty. Only the mean power estimate after this integration period is of interest, so a traditional radiometer will not record information within an integration period. In addition, the use of large bandwidth channels is desired in order to further reduce uncertainty in the estimate of mean power. Because naturally emitted thermal noise varies very slowly with frequency in most cases, measurements from channels with similar center frequencies are deemed identical, and single channel observations are sufficient to represent a large portion of the spectrum.

The addition of RFI to the observed channel violates the noise-only assumption, and causes serious problems for a traditional radiometer. Although interference can take a variety of forms, in many cases RFI can be expected to be localized either in time (i.e. pulsed type interference) or frequency (narrowband interference), or in both domains. If only a small number of such "localized" interfering sources are present, a large portion of either the observation time or bandwidth may contain no interference. However, the traditional radiometer is unable to separate the corrupted and uncorrupted portions of the observation, and therefore may produce corrupted data even with only limited RFI. Because RFI will always increase the mean power when compared to that of the geophysical background, post-processing of the data can be applied to eliminate abnormally high observations. However, lower level RFI can be difficult to separate from geophysical information, making parameter retrievals problematic. Note that an interferer with a large amplitude but small temporal duty cycle and/or small bandwidth can appear as low level RFI when averaged over time and frequency.

A simple way to extend the RFI mitigation capabilities of the traditional radiometer is to increase either the temporal sample rate or the number of frequency channels in the system. These approaches can be implemented in an analog fashion by simple extensions of the traditional radiometer, and the complete data set recorded for post-processing to eliminate RFI at finer temporal and spectral resolution. However, the number of channels that can be implemented using an analog approach is limited, given that additional hardware must be added for each new channel. The temporal sampling rate that can be achieved is also limited by both the RF hardware and the data acquisition subsystem, since the amount of data to be stored eventually becomes unmanageable. Use of digital receiver technologies can address some of these issues: the implicit high temporal sampling rate of a digital receiver allows temporally localized sources to be resolved. In addition, an FFT operation can be performed in real time to obtain a much larger number of frequency channels than is possible using analog sub-channels. However, the data rate of such a system is also much larger than that of the analog approaches. To reduce the data rate, an RFI mitigation processor can be added to the digital receiver to implement simple time and/or frequency domain mitigation algorithms in real time. The resulting "RFI-free" data is then integrated over time and/or frequency to produce a manageable final output data rate. The digital receiver developed at Ohio State is based on such an architecture.

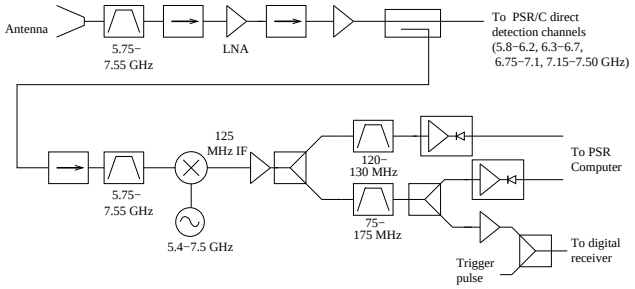

Fig. 1. Simplified block diagram of PSR/CXI front end and downconverter stages

III. System Block Diagram

The PSR/CX instrument of NOAA/ETL has been deployed in several previous airborne remote sensing campaigns [9]-[10], and provides well calibrated brightness measurements along with a variety of possible scanning patterns during flight operations. For the experiments of this paper, a new downconverter section was added to the PSR/CX system; the modified radiometer including the downconversion section is referred to as PSR/CXI in what follows.

Figure 1 is a simplified block diagram of the RF and downconverter sections of PSR/CXI. These components are located inside a sophisticated positioner in the aircraft to allow a high degree of control over the antenna look direction while keeping all components in a temperature controlled enclosure. The front end filter has upper and lower 3 dB cutoff frequencies of 5.75 and 7.55 GHz, respectively; the filter has only 3 poles so the roll off beyond these frequencies is relatively slow. This wide filter enables measurements to be performed over a range of C-band frequencies. Although only a single antenna input is illustrated for simplicity, the PSR/CXI radiometer observes both vertically and horizontally polarized brightnesses. Internal calibration sources are also omitted in Figure 1 for simplicity.

Following the initial filtering and gain components, a portion of the input is coupled off to a new downconversion stage of the PSR/CXI. The remainder of the input is passed on to the existing PSR/CXI direct detection receiver [7], which operates with four analog sub-channels (5.8-6.2, 6.3-6.7, 6.75-7.1, and 7.15-7.5 GHz) and provides dual polarized observations in all sub-channels, with fully polarimetric observations in the 6.75-7.1 GHz sub-channel. These multiple sub-channels provide some measure of RFI mitigation, as discussed in Section VI, but remain large analog channels ($\sim$400 MHz bandwidth) compared to the bandwidth of likely RFI sources. These channels are referred to as PSR "main channels" one through four in the remainder of this paper.

To reduce the possibility of out-of-band interference, the downconversion stage first passes the incoming signal through a filter with a 3 dB bandwidth identical to that of the front-end filter, but with a much more rapid out-of-band cutoff (eight poles as opposed to three in the front end filter).

The downconversion step utilizes an image reject mixer that provides a minimum of 20 dB upper-sideband rejection. The IF center frequency is 125 MHz, and the local oscillator is capable of tuning from 5.4 to 7.5 GHz. The IF output is amplified and then filtered to both 10 MHz and 100 MHz bandwidths. Both these outputs are passed through a logarithmic amplifier/detector, power integrated, and recorded by the PSR computer. The 100 MHz channel is also passed through a linear amplifier, and a portion of this signal is coupled to CISR, while the remainder is detected, power integrated, and recorded by the PSR computer (PSR post-amplification section not shown in Figure 1.) Although the PSR/CXI samples and records both horizontal and vertical polarizations after the linear amplifier, only the vertical channel is passed on to CISR. Because the CISR system described in the next section provides higher spectral and temporal resolution than the 10- and 100 MHz analog channels of PSR, tuned channel results recorded by the PSR computer will not be discussed further in this paper. Additional discussion of results from these channels is provided in [11].

Final observations with the 100 MHz channel cover the range 5.5 to 7.7 GHz. A total of 22 100 MHz channels result; these channels provide tuned observations throughout C-band without requiring a dramatic increase in receiver hardware. These channels are referred to as PSR "tuned channels" in what follows.

IV. Digital Receiver (CISR)

A. CISR capabilities

Digital backends for RFI mitigation in microwave radiometry have been under development at The Ohio State University since 2002 [12]-[16]. A block diagram of the CISR digital backend is illustrated in Figure 2; this backend is physically located in a rack in the aircraft cabin. The CISR digital receiver measures the incoming 100 MHz bandwidth of a PSR tuned channel through the use of two 10-bit, 200 mega-sample-per-second (MSPS) analog-to-digital converters (ADCs). The choice of 10 bits in the ADC components is designed to retain high dynamic range so that large RFI sources will not produce saturation. Each ADC is used to sample 50 MHz of the incoming bandwidth from 125-175 MHz; the 75-175 MHz IF bandwidth accordingly is split into 75-125 MHz and 125-175 MHz channels. The latter is directly passed to a CISR ADC, while the former channel is upconverted to 125-175 MHz before being sampled.

Processing of the sampled data is implemented in field-programmable-gate-array (FPGA) hardware, allowing flexibility in the RFI algorithms to be applied. The current procedure digitally filters each of the ADC outputs to 50 MHz, then combines the channels into a 100 MHz bandwidth signal sampled into I/Q data at 100 MSPS (10 nsec resolution). This first processor stage is referred to as the "digital IF" (DIF) processor. The first RFI mitigation strategy, referred to as "asynchronous pulse blanking" (APB), is implemented with the DIF in a single FPGA. The APB algorithm attempts to remove high amplitude temporal data in real time through a simple detection and blanking procedure; see [14]-[16] for

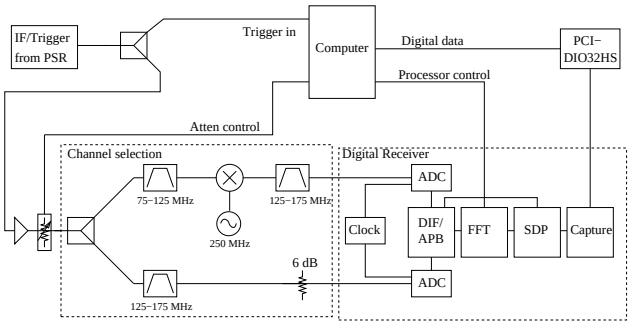

Fig. 2. Simplified block diagram of digital receiver

detailed information. Outputs of the DIF/APB component are then passed through a 1024 point FFT operation, so that 1024 $\sim$ 100 kHz channels are obtained approximately every 10 microseconds. FFT outputs are passed through a detection operation and integrated for a user-controllable time period in an FPGA component referred to as the "spectral domain processor" (SDP). The SDP processor also has the capability of performing a "max-hold" operation on the incoming data instead of integration. Finally, a "capture card" is included for facilitating data transfer through a high-speed digital I/O card (National Instruments PCI-DIO-32HS) to a data recording and control computer.

To increase flexibility in the digital receiver, an ethernet interface was implemented to each FPGA component for setting parameters of the suppression algorithms. This interface allows the APB, FFT, power detection, and/or max-hold/integration operations to be begun or suspended by the control computer as the receiver is in operation. Although a variety of observational modes are possible, the basic configurations of interest are

- Mode 0: Integration, APB off
- Mode 1: Integration, APB on
- Mode 2: Max-Hold, APB off
- Mode 3: Max-Hold, APB on
- Mode 4: Capture

Varying the APB status enables the effectiveness of the APB algorithm to be investigated. The max-hold configurations are of interest because these operations are typically much more sensitive to time localized RFI than integration. However, results from these modes are omitted in this document to simplify the discussion. The final "capture" mode refers to passing through raw DIF data without implementing APB, FFT, or SDP algorithms. Because no integration occurs in the capture mode, the data rate is extremely large, and the resulting duty cycle of observations low. However this configuration (temporal sampling of the incoming field at 10 nsec resolution) can be extremely useful for identifying temporal properties of RFI sources.

In what follows, CISR data will be presented primarily in terms of 1024 point spectra obtained from within a single PSR tuned channel. These results will be grouped according to the PSR tuned channel from which they originate, and labeled as "CISR channel 1-22" results, even though each such channel

contains 1024 sub-channels.

B. Interface to PSR/CXI

Because it is the PSR/CXI data acquisition computer that controls oscillator tuning in the downconverter, the CISR and PSR/CXI computers must be interfaced. To make this interface as simple as possible, a simple 1-bit "trigger" signal was used. This TTL-level pulse is sent from the PSR/CXI control computer to the CISR computer whenever a tuning operation has been completed and measurements should begin. In addition, both computers include highly accurate on-board clocks, synchronized through the IRIG-B standard, so that knowledge of the local oscillator frequency for a particular CISR measurement is obtainable by matching times to the recorded PSR/CXI data.

V. Experiment Description

A. Instrument configuration

Only data for which both CISR and PSR/CXI information was available are discussed here, in particular only the vertically polarized C-band measurements. As stated previously, the PSR/CXI instrument also recorded 100 MHz tuned horizontally polarized channels, but these were not sampled by CISR during the flight. The majority of the data to be presented were obtained from conically scanned observations (i.e. the antenna is rotated in azimuth at a fixed speed) at a fixed incidence angle of 55 degrees from nadir (when in level flight). One set of observations in "stare" mode is also presented; in this case, the antenna is maintained at a fixed, forward-looking azimuth angle, again at a fixed incidence angle of 55 degrees. The antenna 3 dB beamwidth is approximately 10 degrees for all observations.

The tuned LO was swept continuously throughout the flight, with each of the 22 channels being observed for approximately 38 msec; a complete sweep of channels required approximately 836 msec. During the 38 msec observation of a particular channel, approximately 20 msec was utilized for antenna observations, while the remainder was utilized to observe internal calibration sources. When in conical scan mode, the PSR/CXI antenna rotation period was typically 2.9 seconds, so that approximately 3.5 sweeps were performed per antenna "scan" (i.e. rotation). The resulting combined spatial and spectral sweeping process makes interpretation of the tuned data somewhat difficult, as will be discussed in Section VI.

The CISR mode (i.e. "average, APB off", etc.) was switched every 4 sweeps, or slightly more than every rotation of the antenna. In CISR modes 0 to 4, a base temporal resolution of 1.3 msec was utilized, with 12 1024 point spectra (either integrated or max-held) obtained in 15.75 msec following each PSR/CXI trigger. In the capture mode, a 128K capture (1.3 msec) was recorded for each PSR/CXI trigger. CISR required approximately 2 seconds to record measured data to the on-board harddrives following a sweep of modes 0 to 4.

B. Calibration of PSR main and tuned channels

The PSR main channel data to be reported was "quick-calibrated" using the external hot and cold loads of the PSR scan head; this procedure is expected to produce brightnesses typically accurate to within approximately 2 K. Standard deviations of 10 msec noise diode measurements after calibration are approximately 0.4 K. Data recorded by the PSR computer from the 100 MHz linear channels can also be calibrated in this fashion, although reduced observation time of the external loads is available per channel due to the continuation of the tuning process during cal target observations. Test examining the noise diode data recorded by the PSR computer for the linear tuned channels showed typical standard deviations of 0.8 K, as should be expected given the smaller bandwidth of these channels. However, for tuned frequencies near the edge of the PSR front-end filter bandwidth (i.e. < 5.8 GHz and > 7.6 GHz), calibration accuracy was much worse and standard deviations increased up to 7 K or higher, due to the reduced system gain at these frequencies.

C. Calibration of CISR data

Calibration of the 1024 CISR channels in a given 100 MHz tuned PSR channel is also affected by both the continual tuning process and reduced gain at the front end band-edges, as well as the fact that CISR observational modes may be switched during a calibration target observation. Calibration of CISR data is primarily of interest initially for the "Average, blanker off" mode, since here the data obtained is similar to standard radiometer observations. Unfortunately, the combination of tuning frequencies and changing CISR modes resulted in reasonable calibrations being obtained only for subsections of the flight described below, as well as for a subset of PSR tuned channels 1-22. Also noise-diode measurements are not available for evaluating CISR calibration performance. However standard deviations of individual channels within the CISR 1024 point spectrum were found to be on the order of 20-30 K, consistent with the reduced bandwidth of these channels. Although this is extremely high when considering geophysical quantities, CISR calibrated data will be used primarily for evaluating the contribution of large, narrowband RFI sources to the PSR main channels. In these situations, the obtained calibration accuracy can remain acceptable.

Due to the limited size of the calibrated CISR data set, CISR data in Section VI will be shown primarily as raw data, with calibrated results presented only in Section VI-C. The small size of the calibrated CISR data set also limits the extent to whichRFI detection and mitigation performance using the digital receiver data alone can be quantified. For this reason, the primary use of digital receiver data in the next sections will be in determining basic properties of the RFI sources observed, as well as in evaluation of the performance of the PSR main channel mitigation algorithm.

D. Flight plan

The observations described in this paper were performed on board a US Navy P-3 research aircraft during a test flight

Time (UTC)	Event	Comments
16:13	Takeoff from WFF	
16:40	Start CISR data collection	Low altitude circles over WFF
16:54	Exit circles over WFF	Start transit to buoy 44009
17:04	Begin hex-cross pattern over buoy	
17:42	End hex-cross pattern over buoy	Prepare for cal-rolls
17:45	Begin set of 3 60 degree cal rolls	
17:52	Finish cal rolls	Begin transit to WFF, stare mode
18:01	Land at WFF	

TABLE I

TIME HISTORY OF TEST FLIGHT ON OCT. 8TH, 2004

on October 8, 2004 prior to departure of the aircraft for the AMSR-E Antarctic Sea Ice (AASI) cal-val campaign on October 9. Table 1 provides information on the portions of the test flight plan to be discussed. Figure 3 illustrates the geographical region observed as well as the flight track; note the Wallops Flight Facility (WFF) and NDBC buoy 44009 are marked with black circles in the Figure. As can be seen in Table 1, the flight plan included low altitude (i.e. approximately 2000 ft and 5000 ft) circles over WFF after takeoff from WFF at 16:13 UTC, followed by a climb to approximately 18475 ft for observations over NDBC buoy 44009 (located approximately 26 km from the shore) in a hex-cross pattern, followed by three steep rolls for PSR observations of the sky, then return to WFF through a gradual descent in "stare mode", landing at 18:01. In Figure 3, the flight portion from WFF to the buoy is along the more northerly path as indicated by the arrows in the Figure, while the return to WFF follows the more southwestern track. Overall the observed data set contains a variety of useful scenes for RFI investigations, including both land and near-coastal regions. The images of PSR/CXI conically scanned data to be illustrated will be presented in terms of time and scan angle; these should not be taken as geographic images given possible variations in the aircraft heading, pitch, roll, and altitude. Although complete geo-location of these data is possible, the relatively simple flight plan allows basic interpretation of these images without significant difficulty.

The following sections present and discuss subsets of the measured data for the major sections of the flight plan, including a portion of the low-altitude circles over WFF, a portion of the hex-cross pattern over the buoy, and a portion of the stare-mode data on return to WFF.

VI. RESULTS

A. Low Altitude Circle over WFF

1) PSR main channel images: Figure 4 illustrates PSR/CXI scan images for the four main channels (5.8-6.2, 6.3-6.7, 6.75-7.1, and 7.15-7.5 GHz, labeled channels 1 to 4 respectively) during a circle at approximately 2000 ft altitude over WFF. The color scale is calibrated brightness temperature in Kelvins, and the forward looking portion of the conical scan is shown. Due to the varying aircraft heading during this circle flight, a direct correlation of the scan image to a geographical image should not be expected. However the image clearly contains

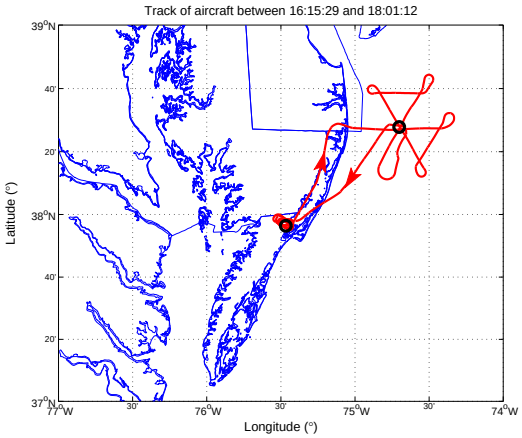

Fig. 3. Regional map of test flight area, including flight track as well as Wallops Flight Facility and NDBC buoy 44009 (black circles)

both land and water observations, with strong RFI evident due to the large differences among channels in some image portions. All four channels contain evidence of RFI at some location, with brightnesses up to 9516K, 3106K, 966K, and 3473K observed in channels 1 through 4, respectively. Channel 3 appears the least corrupted of the channels.

Using data from the four PSR main channels, it is possible to attempt to remove RFI using the algorithm described in [7]. This algorithm consists of a series of chi-squared and threshold tests, successively labeled the "four-point tests", "three-point tests", and so on in what follows. Each test is based on both a brightness thresholding procedure as well as examination of a least-squared-error linear fit to the observed brightnesses versus frequency. If a particular test is passed, the algorithm exits, and typically replaces brightnesses deemed corrupted with the prediction from the accepted linear fit. More specifically, steps in the algorithm are:

- Four point test: Test is failed if
  - any of the four brightnesses are outside a specified range R, or
  - the absolute value of the slope of a linear fit to all four channel brightnesses exceeds a threshold S, or
  - the total squared error of the linear fit exceeds a threshold E.

  The algorithm exits if the test is passed, and no channels are deemed corrupted. Otherwise proceed to three point test.
- Three point test: Four sub-tests are performed:
  - In each sub-test, a three point least squares fit is performed to the brightness data with one of the four channels removed.
  - Conditions for failing a sub-test are identical to those for failing the four point test, including the threshold test applied to the three channels utilized.
  - The sub-test is also failed if the point not utilized in the linear fit has a brightness less than that predicted by the linear fit minus a threshold D
  - Three point test is failed if no sub-test is passed.

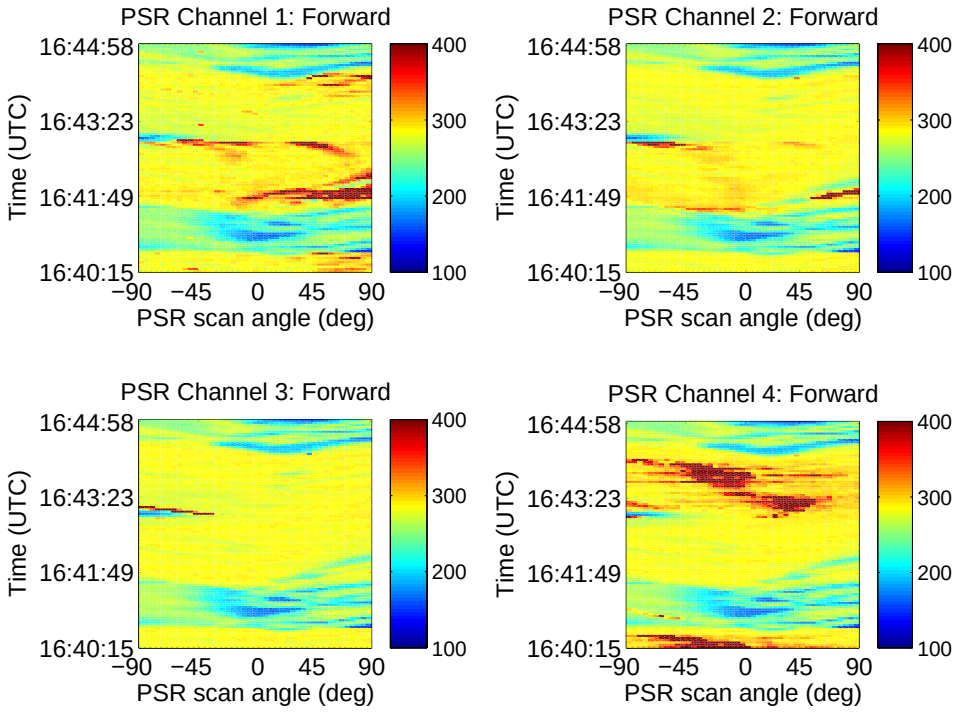

Fig. 4. Calibrated brightnesses observed in 4 PSR main channels for forward looking portion of a 2000 ft altitude circle over WFF

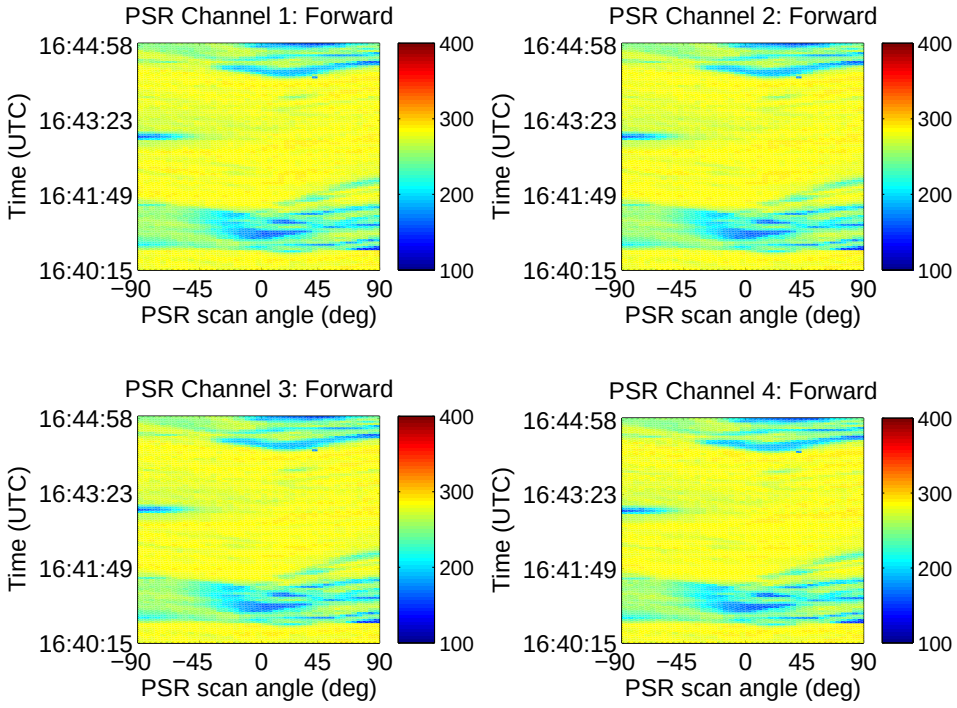

Fig. 5. "RFI corrected" brightnesses from Figure 4

  - If one or more sub-tests are passed, the sub-test with the minimum squared error in the linear fit is chosen, and the excluded channel from that test declared corrupted.
  - Brightness of corrupted channel is replaced by prediction from the linear fit
- Two point test: Six possible pairs of points among the four channels are examined in six sub-tests:
  - In each sub-test, a two point linear fit is performed to the selected pair of brightnesses
  - Conditions for failing a sub-test are identical to those for failing the four point test; note the total squared error is always zero in this case
  - The sub-test is also failed if either or both of the points not utilized in the linear fit have brightnesses less than the average of the two selected brightnesses minus a threshold D
  - Two point test is failed if no sub-test is passed.
  - If one or more sub-tests are passed, the sub-test with the smallest brightness difference between the two selected channels is chosen, and the excluded channels from that test declared corrupted.
  - Brightness of corrupted channels are replaced by the average of the two selected channel brightnesses
- One point test: Choose channels with brightnesses in the range R. Replace all channel brightnesses with the minimum of these in-range brightnesses. If no channel has a brightness in the range R, flag all channels as corrupted.

Figure 5 plots the PSR main channel images from Figure 4 after this algorithm has been applied. Parameters utilized were 130 to 310 K for the range R, 3 K/GHz for the slope threshold S, 3.38 K for the fit error threshold E, and 1.3 K for the deviation D. Note the latter two parameters should be proportional to the expected standard deviation of the observed brightnesses when used for other datasets. Results show a dramatic reduction of obvious RFI, and detailed examination shows the capabilities of this algorithm at detecting and removing RFI even on the scale of a few K. In the 4576 pixels of Figure 4, the algorithm concludes that only 12.5% contain no interference, while 27.5% have one sub-channel corrupted, 27% have two sub-channels corrupted, and 33% have three or more sub-channels corrupted. While these specific numbers depend strongly on the algorithm parameters utilized, as well as the accuracy of the PSR quicklook calibration, it is clear that the image of Figure 4 contains a significant amount of RFI, and that the sub-channel algorithm is relatively successful in detecting and removing this RFI. However, results will be shown in Section VI-C to illustrate the limitations of this algorithm when all four main channels simultaneously contain RFI contributions.

2) CISR data: In order to examine CISR data from the 22 tuned channels, the effects of LO tuning must be considered. It should be noted that the possibility exists for the tuned channels to fail to observe RFI recorded by the PSR main channels because the local oscillator was not tuned for the RFI frequency when the source was in the antenna pattern. Also, it is not possible to form scanned images similar to those of Figure 4 for these channels because each image pixel is recorded at a different center frequency in the tuning process. While it is possible to examine the time history of a specific CISR channel, successive measurements of a given channel can be time separated by as much as 836 msec, again making correlation of a channel time history to the PSR main channel scan images difficult.

To address this issue, an interactive data analysis tool (IDAT) was developed. This tool overlays symbols on the main PSR channel scan images that indicate the tuned channel observed in a particular image pixel. It is then possible for the user to select a pixel and examine the particular PSR tuned channel and CISR measurements corresponding to that pixel. The connection between the PSR and CISR channel time histories is thus established through this tool.

Although IDAT makes it possible to examine possible sources of RFI observed in the PSR main channel images, it is not possible to demonstrate use of this tool in a paper document. For this reason, CISR data will be illustrated through time history plots, with IDAT results reported in the discussion.

CISR spectra time histories are presented as color images, with frequency on the horizontal axis and "sample number" on the vertical axis; data in the plots represent the mean of the 12 1.3 msec spectra acquired after a PSR "trigger". While not contiguous in time due to both LO tuning (short time delays) as well as changes in the CISR mode (longer time delays), the time histories illustrated do occur within the time period of the corresponding PSR main channel image.

Due to the difficulties with calibration of all CISR data, results are presented in terms of data divided by its mean over the corresponding set of samples. This mean is actually computed over the lower 90% of samples only in an attempt to remove any RFI induced bias effects on the mean value used in the normalization. These normalized data are then converted to decibels in the images shown; a value of zero decibels throughout the image indicates no deviation from the mean, while other values can indicate significant deviations typically caused by RFI, but also potentially caused by geophysical brightness changes. However, RFI effects are readily detected due to their localized behavior in frequency as opposed to geophysical effects.

CISR "average, blanker off" spectra are illustrated in Figure 6 for a subset of the 22 tuned channels; channels excluded from the figure did not show obvious RFI contributions on the scales utilized for the figure. Strong wideband interferers are observed near 6190 MHz and 7480 MHz, while more narrowband sources occur at several frequencies. In some cases, these sources are obvious in multiple "samples" in the image, while in others, they are obvious only in a small subset of samples, or even only one sample. A few low-level geophysical variations are also observed, corresponding to a near-uniform brightening or darkening of the image in a given sample; analysis using the IDAT tool shows these effects to be related to the land and water portions of the image. It is also noted that CISR results near the channel lower and upper frequencies (i.e. left- and right-edges of each plot) as

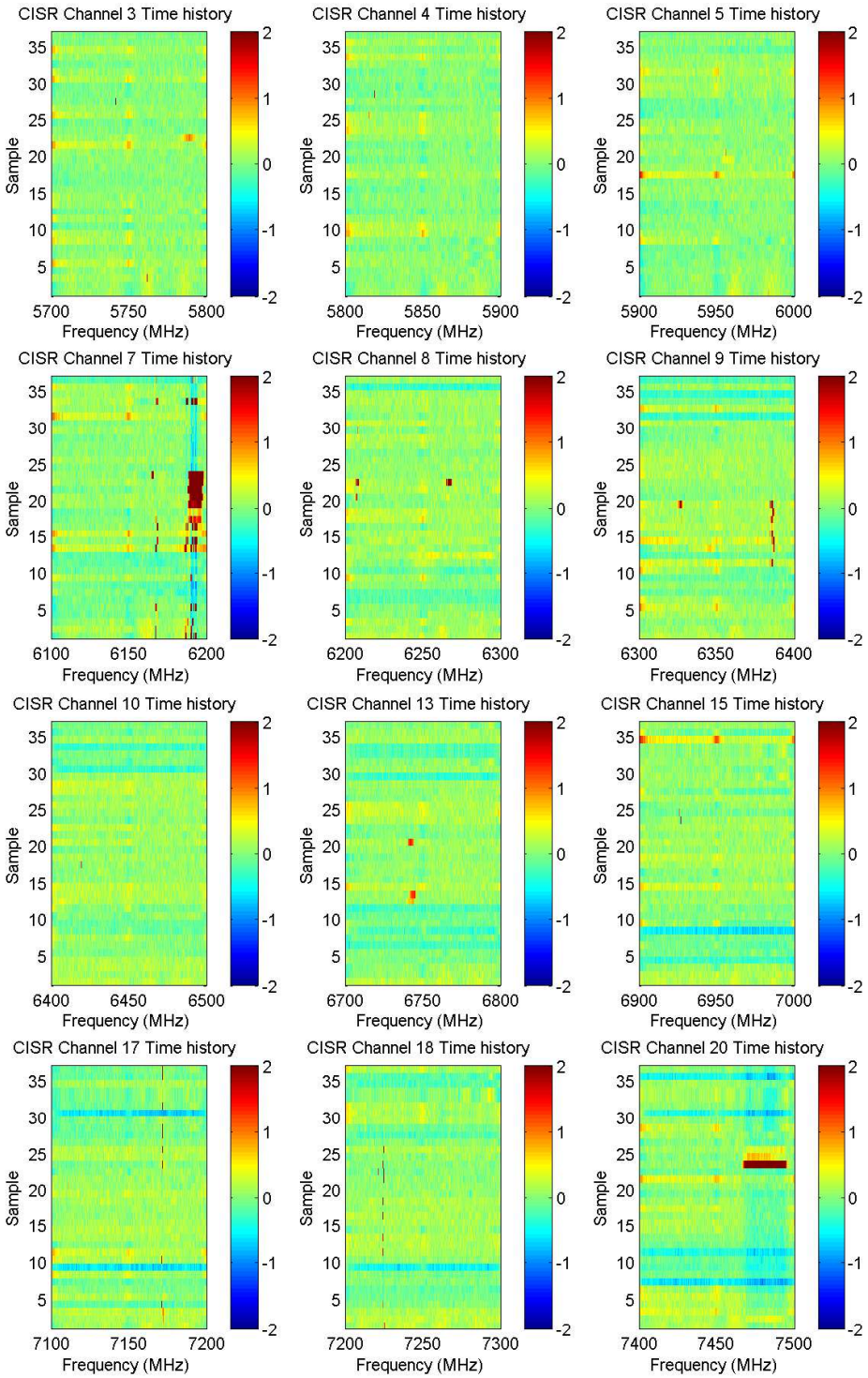

Fig. 6. Time histories of selected CISR normalized spectra corresponding to PSR main channel images in Figure 4

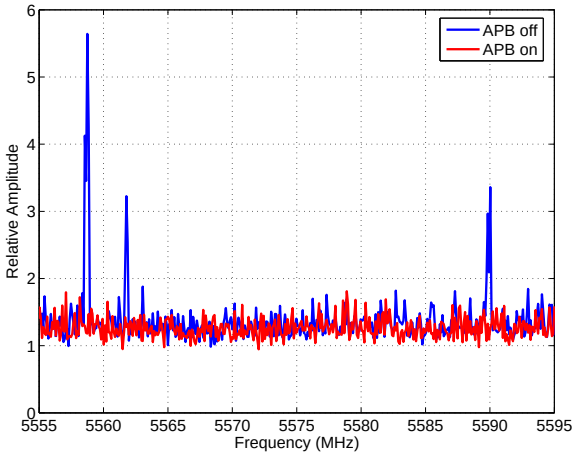

Fig. 7. Ratio of maximum to mean CISR channel results in a portion of tuned channel 1, for the dataset of Figure 6

well as at the band center (i.e. 50 MHz from the left-hand frequency in a given plot), experience more variation due to reduced CISR IF gain near these locations. Overall however, these images are useful for interpreting properties of the RFI sources encountered in the PSR main channel images.

Analysis with the IDAT tool shows the 6190 MHz source to be correlated to the strong RFI in PSR main channel 1 at times near 16:40:15, 16:41:49, and 16:44:00. CISR observed sources at 6207 and 6265 MHz appear correlated to the PSR main channel 1 and 2 images around time 16:43:00 as well. Sources at 6387 and 6740 MHz are related to the PSR main channel 2 RFI response around 16:41:30, while the wideband source at 7480 MHz appears in the PSR main channel 4 image at times from 16:43 to 16:44. Narrowband sources near 7171 MHz and 7224 MHz produce smaller observable contributions in both the PSR main channel 3 and 4 images, particularly in the water portions of these images at times 16:40:15 to 16:41:49.

CISR results from the "average, blanker on" mode were also examined for this dataset. In most cases, little difference between the "blanker on" and "blanker off" results were observed, suggesting that the majority of the RFI sources encountered are not pulsed transmissions. However, "blanker on" results in tuned channels 1 and 2 were found to show a reduction in RFI compared to the "blanker off" mode. Figure 7 plots a comparison of "blanker on" and "blanker off" results for this portion of the flight, in a subset of tuned channel 1 frequencies. To emphasize pulsed transmission effects, these results are illustrated in terms of the maximum of the 1.3 msec CISR data in a given bin, divided by the mean of those data. Results clearly demonstrate a dramatic reduction in RFI sources near 5558, 5562, and 5590 MHz, suggesting that these sources are pulsed transmissions. Further analysis of the CISR "capture" mode data confirmed the pulsed-nature of these transmissions; location of pulsed sources in this portion of C-band ($<$ 5.7 GHz) is consistent with U. S. frequency allocations [17].

Further interpretation of these results can be obtained through a comparison of CISR observations with a database of known emitters in this area [6]. Although only an initial examination has been performed at this point in time, it appears that the majority of the observed sources are consistent with properties known from their registrations. Additional studies regarding such database "matchups" are currently in progress.

B. Portion of Hex-Cross Lines over Buoy

Figure 8 illustrates PSR main channel brightnesses for a portion of the hex-cross overflight of NDBC 44009. This portion of the flight follows a northwestward track and includes the buoy location; the aircraft heading was approximately uniform during the period of the image shown, and the altitude was approximately 18,475 ft. For this sea scene, strong RFI (up to 834K in channel 1, 488K channel 2, and 499 K in channel 3) is still observed. Analysis of the PSR data following geolocation shows these sources apparently to be located on ships in these heavily used shipping lanes, as well as continued reception of land-based sources. PSR images after applying the four channel RFI removal algorithm are not shown, but performance is similar to that of Figure 5 in that all obvious RFI sources and even apparent low-level sources of a few K are detected and removed by the algorithm. In this case, the reduced level of RFI in channel 4 is obvious, and the level of RFI detected in this channel (though up to 16.5 K in some cases) is dramatically less than in the other main channels. The sub-channel algorithm classifies only 2% of the examined 4312 pixels as RFI-free, while 8.25%, 39.75%, and 50% are classified as containing RFI in one, two, or three-or-more sub-channels. Again these specific numbers are highly dependent on the algorithm parameters utilized, but it is clear that the scene considered contains significant RFI corruption.

CISR normalized spectral plots in Figure 9 show a large number of wideband sources located from 6 to 6.4 GHz, along with wideband sources near 6850 and 6930 MHz. The relatively uniform spacing of wideband sources observed from 6 to 6.4 GHz suggests a set of communications channels, each of approximately 25 MHz bandwidth. Again these observations appear consistent with properties of registered sources in the area. Narrowband sources are observed at numerous frequencies, again sometimes in a large number of temporal

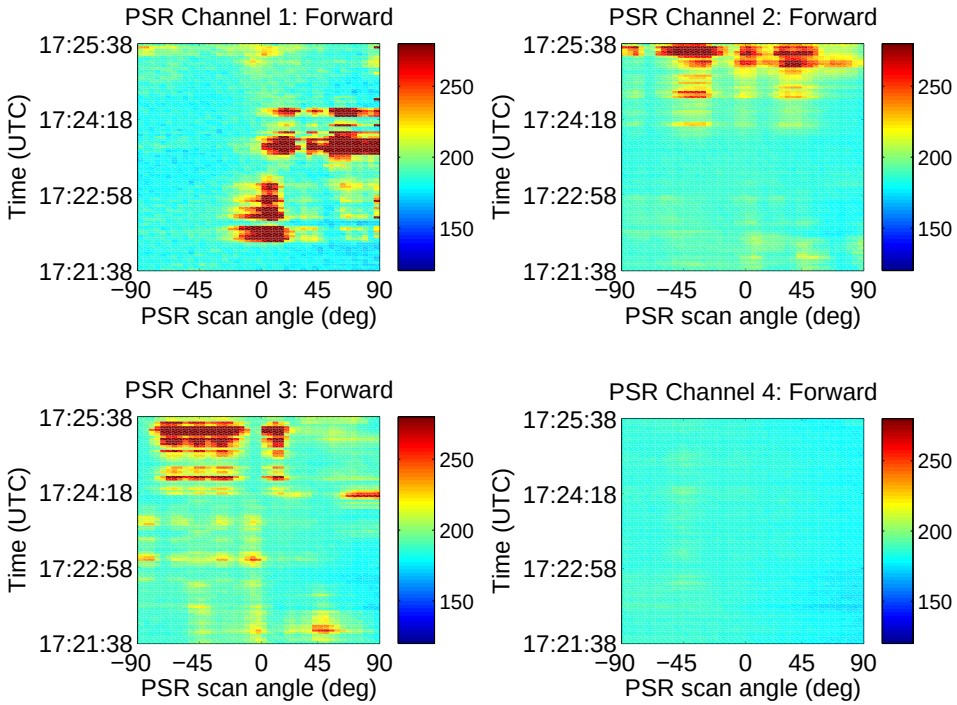

Fig. 8. Calibrated brightnesses observed in 4 PSR main channels for forward looking scan of portion of hex-cross flight over NDBC buoy 44009

samples and sometimes in only a small set (or even one) sample. The single large response observed in channel 2 again is reduced in blanker on observations, and is therefore believed to be a pulsed source.

Analysis with the IDAT tool shows the large brightnesses in PSR main channels 1 and 2 to be correlated primarily to the wideband sources below 6.3 GHz (for PSR main channel 1) and from 6.2 to 6.7 GHz (for PSR main channel 2). The narrowband sources from 6750 to 6850 MHz, as well as the wideband source at 6850 MHz, contribute to the larger PSR main channel 3 brightnesses observed in the earlier part of image. CISR results for tuned channels 18 to 22 do not show obvious RFI contributions on the scales of the images shown, as should be expected from the reduced level of RFI in the PSR main channel 4 image. However, the narrowband source observed near 7130 MHz in Figure 9 does produce low level contributions to this channel that are not easily removed by the four channel algorithm. Further discussion of this situation is provided in the next section.

C. Stare Mode During Transit back to WFF

The "stare mode" data obtained during transit from the at-sea measurements back to WFF offer interesting possibilities for analysis. These data are advantageous in that no scanning of the antenna is performed, so that a sweep of spectrometer channels can observe similar geographical locations if the aircraft velocity is moderate. Here data from this portion of the flight is used to highlight the advantages of the digital receiver system in detecting and removing RFI contributions; only a small subset of the measured data is illustrated.

Sample PSR main channel data is shown as a line plot in Figure 10; this approximately four second portion of the data was taken during descent to the WFF airport at altitudes decreasing from 2700 to 2500 ft. This portion of the flight occurs over the Chincoteague Bay, and includes an all sea scene. Strong RFI contributions are observed in channels 1 and 2, with brightnesses larger than 180 K, while brightnesses in the other channels are in the more reasonable range of approximately 165 K. Also included in this plot are results following the PSR RFI removal algorithm; the algorithm detects RFI in channels 1 through 3, and therefore replaces all channel brightnesses with those obtained from channel four. Although this is considered a failure of the algorithm, these results illustrate the possibility of simultaneous RFI corruption of three or more of the PSR main channels.

Analysis of CISR data similar to that illustrated previously can be used to detect and classify the RFI sources that contribute to PSR main channels one through three. Properties of the sources observed are similar to those reported earlier. However, in this case, a large narrowband source near 7110 MHz is also observed; this source is located near the PSR channel four 3 dB band edge of 7.15 GHz. For this particular portion of the flight, an acceptable calibration of the CISR data is available; Figure 11 plots CISR calibrated brightnesses for the "average, blanker off" mode in a portion of tuned channel 17. This data corresponds to the location of the vertical line marked in Figure 10. The narrowband source near 7110 MHz when resolved in frequency is observed to produce a brightness of approximately 2600 K, easily classifiable as RFI. An estimation of the effect of this source on PSR channel four can be obtained by computing the mean brightness of the CISR spectrum with and without this source; here the region between the two vertical lines in Figure 11 is excluded in the latter case. Results show this source to contribute on the order

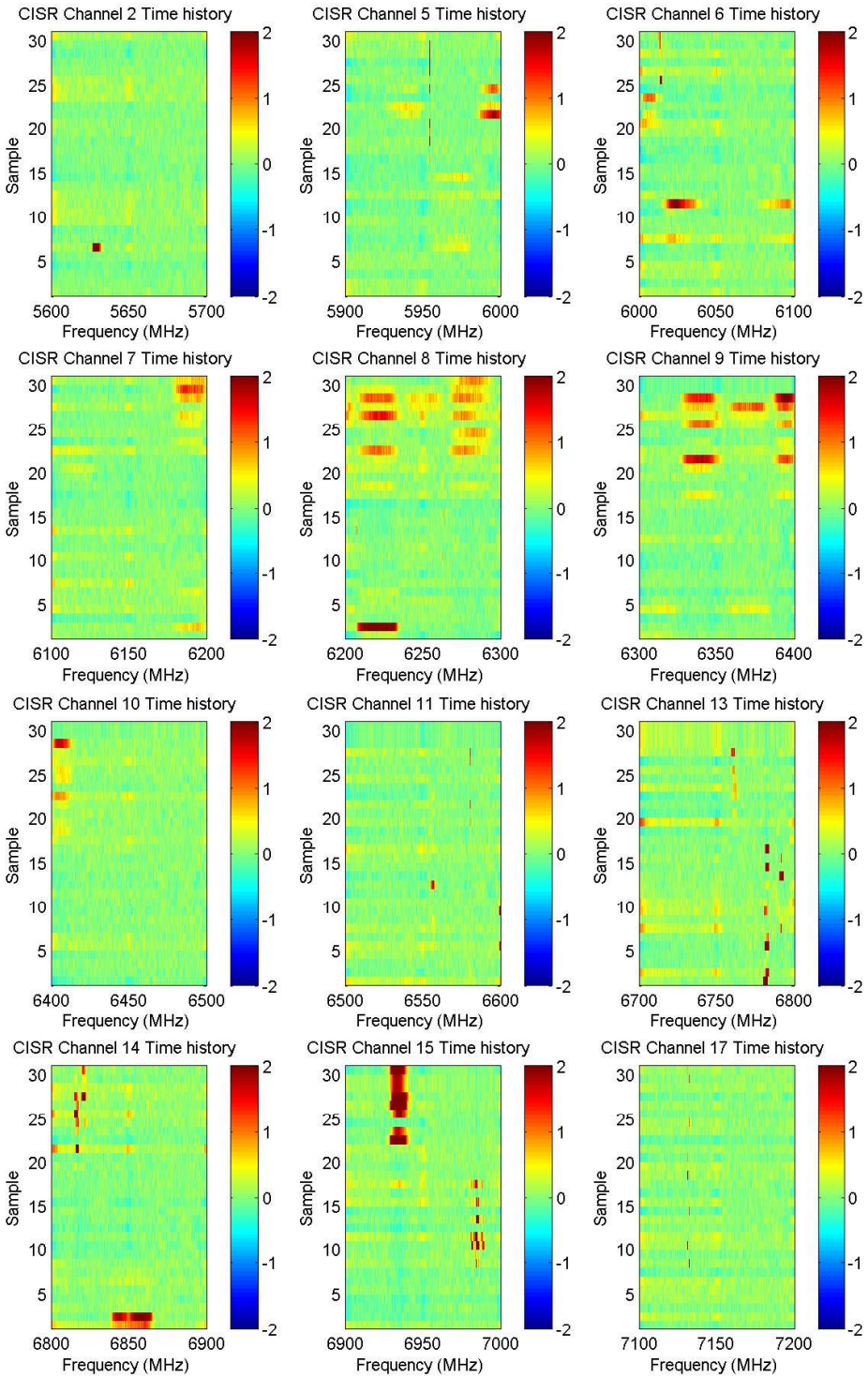

Fig. 9. Time histories of selected CISR normalized spectra for portion of flight shown in Figure 8

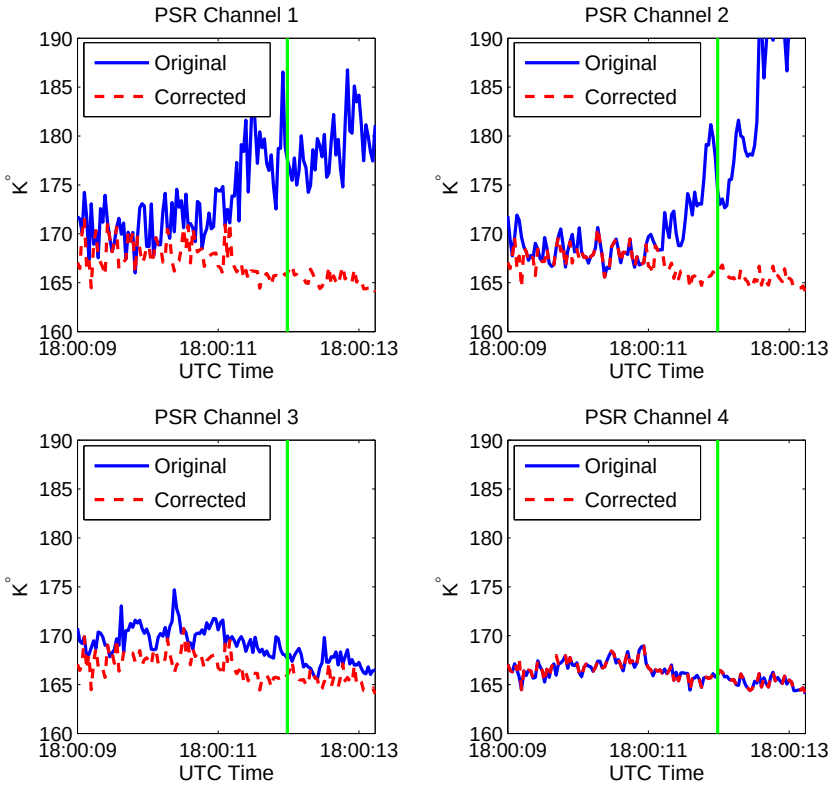

Fig. 10. "Stare mode" PSR main channel data during descent to WFF; results are shown before and after the PSR RFI mitigation algorithm is applied. Vertical line near time 18 : 00 : 12 marks the time of the data illustrated in Figure 11.

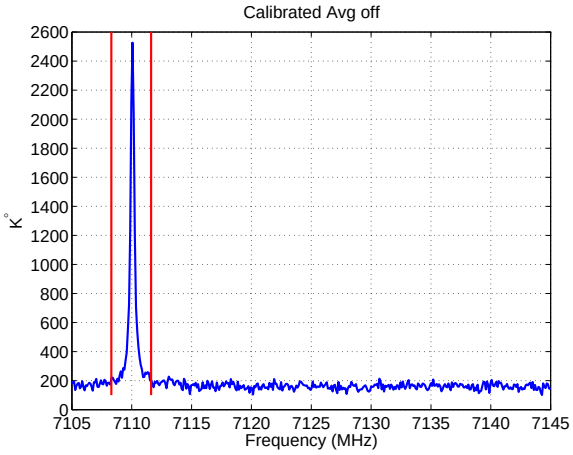

Fig. 11. Calibrated CISR data from tuned channel 17 at the location of the vertical line in Figure 10; the vertical lines here mark the frequency boundaries within which an RFI source is "detected"

of 3 K to PSR main channel four. In this case, the retention of the channel four brightness by the PSR RFI removal algorithm is in error, but this error is not easily detected due to the low-level nature of the RFI source. However, when resolved in frequency by the digital receiver, this source is easily classified as RFI and can be removed.

VII. Conclusions

Joint deployment of the PSR/CXI and CISR systems has provided a useful dataset for detailed examination of RFI sources and mitigation techniques at C-band. The joint dataset contains observations of a variety of scenes, including strong and weak RFI environments. The data clearly show the possibility of significant corruption of measured brightnesses for wideband channels throughout C-band, with the higher frequencies typically observing less but still appreciable corruption. Although the multiple sub-channel removal algorithm of the PSR was found generally to perform well, cases existed where RFI contributions occurred in all sub-bands, so that correction was no longer possible. This is a particular problem when at least one of these bands contains only low-level RFI, so that it may be mis-classified as containing a geophysical brightness, eventually leading to parameter retrieval errors.

Though issues with the experimental configuration precluded a detailed quantitative study of the RFI removal performance achieved by the digital receiver, the data obtained nevertheless demonstrated qualitatively the advantages of the digital receiver's higher spectral resolution. It is clear that a large fraction of the RFI sources observed should be able to be detected and removed easily given the digital receiver's high spectral resolution. Additional analyses are in progress to further quantify the RFI detection and mitigation effectiveness of the digital receiver, and to determine the ability to which the RFI environment can be forecast through knowledge of registered emitter properties.

Continued deployment of the system is also planned in order to provide observations over a wider range of environments; future campaigns will utilize a slower scan rate for the antenna, as well as a smaller number of CISR modes in order to allow improved calibration of digital receiver data. Inclusion of additional digital backends which utilize "moment detection" strategies for RFI detection [18] are also planned in future deployments. Such strategies may yield superior detection performance to enhanced time/frequency resolution for wideband sources producing low-level, noise-like emissions (such as those currently under development for "ultra-wideband" communications systems). It is hoped that results from these studies will guide development of improved RFI detection and mitigation technologies for future spaceborne microwave radiometers.

References

[1] Wende, C. D., "NASA remote sensing and frequency issues," *IGARSS'00*, conference proceedings, 2000.

[2] Njoku, E. G., P. Ashcroft, T. K. Chan, and L. Li, "Global survey and statistics of radio-frequency interference in AMSR-E land observations," *IEEE Trans. Geosc. Rem. Sens.*, vol. 43, pp. 938–947, 2005.

[3] Ellingson, S. W. and J. T. Johnson, "A polarimetric survey of radio frequency interference in C- and X-bands in the continental United States using WindSat radiometry," accepted by *IEEE Trans. Geosc. Rem. Sens.*, 2005.

[4] Li, L., P. W. Gaiser, and M. Bettenhausen, "WindSat radio frequency interference signature and its identification over land and ocean," submitted to *IEEE Trans. Geosc. Rem. Sens.*, 2005.

[5] Kunkee, D. B., N. S. Chauhan, and J. J. Jewell, "Phase one development of the NPOESS Conical-scanning microwave imager/sounder (CMIS)," *IGARSS'02* conference proceedings, 2002.

[6] Kunkee, D. B., N. S. Chauhan, and J. J. Jewell, "Spectrum management for the NPOESS Conical-scanning microwave imager/sounder (CMIS)," *IGARSS'02* conference proceedings, 2002.

[7] Gasiewski, A. J., M. Klein, A. Yevgrafov, and V. Leuski, "Interference mitigation in passive microwave radiometry," *IGARSS'02* conference proceedings, 2002.

[8] Fridman, P. A. and W. A. Baan, "RFI mitigation methods in radio astronomy," *Astronomy and Astrophysics*, vol. 378, pp. 327–344, 2001.

[9] Piepmeier, J. R., and A. J. Gasiewski, "High-resolution passive microwave polarimetric mapping of ocean surface wind vector fields," *IEEE Trans. Geosc. Rem. Sens.*, vol. 39, pp. 606-622, 2001.

[10] Jackson, T. J., A. J. Gasiewski, A. Oldak, M. Klein, E. G. Njoku, A. Yevgrafov, S. Christiani, and R. Bindlish, "Soil moisture retrieval using the C-band polarimetric scanning radiometer during the Southern Great Plains 1999 Experiment," *IEEE Trans. Geosc. Rem. Sens.*, vol. 40, pp. 2151-2161, 2002.

[11] E. McIntyre, A. J. Gasiewski, V. Leuski, M. Klein, B. Weber, V. Irisov, and B. Stankov, "An interference mitigation technique for passive remote sensing of soil moisture," *IGARSS'05*, conference proceedings, 2005.

[12] Ellingson, S. W. and G. A. Hampson, "Mitigation of radar interference in L-band radio astronomy," *Astrophys. Jour. Suppl.*, vol. 147, pp. 167–176, 2003.

[13] Ellingson, S. W., G. A. Hampson, and J. T. Johnson, "Design of an L-band microwave radiometer with active mitigation of interference," *IGARSS'03* conference proceedings, 2003.

[14] Johnson, J. T., G. A. Hampson, and S. W. Ellingson, "Design and demonstration of an interference suppressing microwave radiometer," *IGARSS 2004*, conf. proceedings, 2004.

[15] N. Niamsuwan, J. T. Johnson, and S. W. Ellingson, "Examination of a simple pulse blanking technique for RFI mitigation" *Radio Science*, vol. 40, Article RS5S03, June 2005.

[16] OSU IIP project document server, `http://esl.eng.ohio-state.edu/~rstheory/iip/docserv.html`.

[17] *United States Frequency Allocation Chart*, National Telecommunications and Information Administration, `http://www.ntia.doc.gov/osmhome/allochrt.pdf`.

[18] Ruf, C. S., S. M. Gross, and S. Misra, "RFI detection and mitigation for microwave radiometry with an agile digital detector," submitted to *IEEE Trans. Geosc. Rem. Sens.*, 2005.